Cell Reports

Article

METTL14 regulates chromatin bivalent domains in mouse embryonic stem cells

Graphical abstract

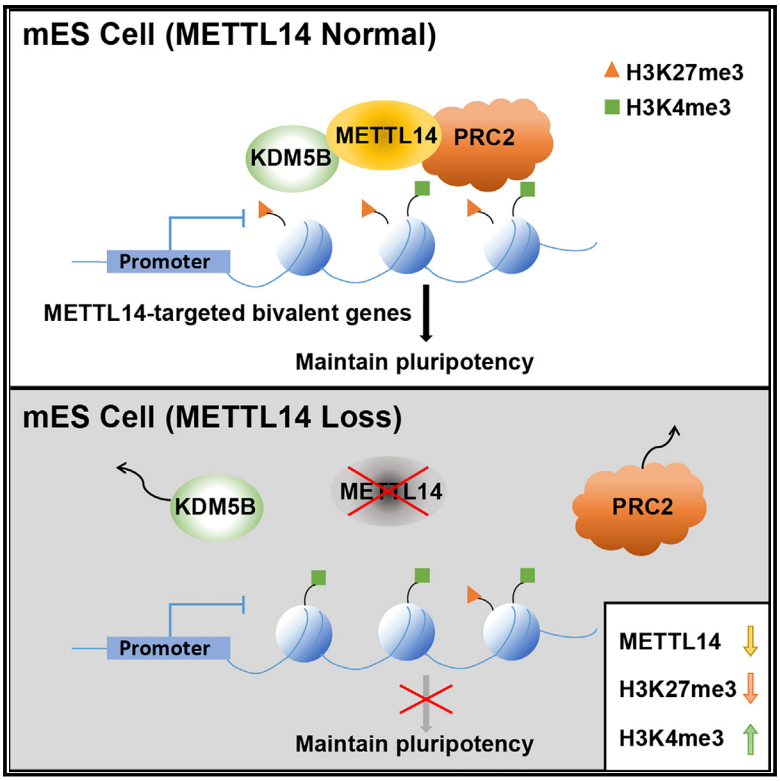

Highlights

- METTL14 mainly localizes to bivalent domains in mouse embryonic stem cells
- METTL14 loss results in H3K27me3 decrease but H3K4me3 increase at bivalent domains
- METTL14 regulates bivalent domain independent of METTL3 or m^{6}A modification
- METTL14 might recruit H3K27me3 methyltransferase PRC2 and H3K4me3 demethylase KDM5B

Authors

Mandi Mu, Xinze Li, Li Dong, ..., Wenqi Xu, Yang Shi, Hongjie Shen

Correspondence

wenqixu@fudan.edu.cn (W.X.), yang.shi@ludwig.ox.ac.uk (Y.S.), hongjieshen@fudan.edu.cn (H.S.)

In brief

Mu et al. show that METTL14 mainly localizes to bivalent domains in mouse embryonic stem cells and regulates bivalency independent of its partner METTL3 or m^{6}A modification. *Mettl14* loss results in decreased H3K27me3 but increased H3K4me3 levels at bivalent domains, possibly through regulation of recruitment of PRC2 and KDM5B.

Mu et al., 2023, Cell Reports *42*, 112650
June 27, 2023
https://doi.org/10.1016/j.celrep.2023.112650

CellPress

Cell Reports

CellPress
OPEN ACCESS

Article

METTL14 regulates chromatin bivalent domains in mouse embryonic stem cells

Mandi Mu,[1] Xinze Li,[1] Li Dong,[1] Jin Wang,[1] Qingqing Cai,[1] Yajun Hu,[1] Duanduan Wang,[1] Peng Zhao,[1] Lei Zhang,[1] Daixuan Zhang,[1] Siyi Cheng,[1] Li Tan,[1,2] Feizhen Wu,[1] Yujiang Geno Shi,[1] Wenqi Xu,[1,2,*] Yang Shi,[3,*] and Hongjie Shen[1,2,4,*]

[1]Longevity and Aging Institute, the Shanghai Key Laboratory of Medical Epigenetics, Institutes of Biomedical Sciences, Zhongshan Hospital, Fudan University, Shanghai, China

[2]Shanghai Pudong Hospital, Fudan University Pudong Medical Center, Fudan University, Shanghai, China

[3]Ludwig Institute for Cancer Research, Oxford Branch, Oxford University, Oxford, UK

[4]Lead contact

*Correspondence: wenqixu@fudan.edu.cn (W.X.), yang.shi@ludwig.ox.ac.uk (Y.S.), hongjieshen@fudan.edu.cn (H.S.)

https://doi.org/10.1016/j.celrep.2023.112650

SUMMARY

METTL14 (methyltransferase-like 14) is an RNA-binding protein that partners with METTL3 to mediate N^6-methyladenosine (m^6A) methylation. Recent studies identified a function for METTL3 in heterochromatin in mouse embryonic stem cells (mESCs), but the molecular function of METTL14 on chromatin in mESCs remains unclear. Here, we show that METTL14 specifically binds and regulates bivalent domains, which are marked by trimethylation of histone H3 lysine 27 (H3K27me3) and lysine 4 (H3K4me3). Knockout of *Mettl14* results in decreased H3K27me3 but increased H3K4me3 levels, leading to increased transcription. We find that bivalent domain regulation by METTL14 is independent of METTL3 or m^6A modification. METTL14 enhances H3K27me3 and reduces H3K4me3 by interacting with and probably recruiting the H3K27 methyltransferase polycomb repressive complex 2 (PRC2) and H3K4 demethylase KDM5B to chromatin. Our findings identify an METTL3-independent role of METTL14 in maintaining the integrity of bivalent domains in mESCs, thus indicating a mechanism of bivalent domain regulation in mammals.

INTRODUCTION

Histone proteins and their post-translational modifications have emerged as important players in the regulation of gene expression and other chromatin-templated processes. Histone H3 lysine 4 trimethylation (H3K4me3) and histone H3K27me3 play important roles in gene activation and repression, respectively, in mouse preimplantation embryos.[1] Chromatin regions composed of both H3K4me3 and H3K27me3 are termed bivalent domains, which are prevalent in mouse embryonic stem cells (mESCs).[2] Genes marked by bivalent domains are generally believed to be in a poised state and can be activated rapidly in response to developmental cues.[2] Accumulating evidence suggests that the polycomb repressive complex 2 (PRC2), which mediates H3K27me3 of chromatin, including bivalent domains, functions as a brake to prevent the premature activation of bivalent genes.[3,4] Recent studies also suggested that H3K4me3 is crucial for keeping these genes from DNA methylation.[5,6] However, how the bivalent domains are established and regulated remains incompletely understood.

Previous studies identified RNA-binding proteins (RBPs) at bivalent promoters,[7] where they regulate H3K27me3.[8,9] METTL14 is an RBP that partners with METTL3 to mediate N^6-methyladenosine (m^6A) modification on both mRNA and non-coding RNAs.[10–15] METTL3/METTL14 also mediates m^6A modification on RNAs transcribed from repetitive elements and nascent RNAs to regulate heterochromatin[16–19] and transcription,[10,11,20,21] respectively. Of the heterodimeric METTL3/METTL14 catalytic core complex, METTL3 mediates catalysis, while METTL14 provides binding to substrate RNA.[22–24] Interestingly, some earlier studies hinted at functions of METTL3 and METTL14 that are potentially independent of each other. For example, depletion of METTL3 and METTL14 in mouse results in different phenotypes in spermatogenesis.[25] In addition, the chromatin-binding sites of METTL3 and METTL14 show distinct profiles and very little overlap in primary embryonic lung fibroblasts[26] and in acute myeloid leukemia (AML) cells,[27] respectively.

Here, we report that in mouse ESCs, in contrast to METTL3, which is enriched at repetitive elements, METTL14 is by and large enriched at genomic regions decorated by both H3K27me3 and H3K4me3, i.e., the bivalent domains. We show that loss of METTL14 leads to a significant and selective reduction of H3K27me3 and an increase of H3K4me3 at these bivalent domains, leading to gene activation, suggesting that METTL14 is important for the integrity of bivalent domains. Mechanistically, METTL14 appears to maintain bivalent domains by promoting the binding of the H3K27me3 writer, the PRC2 complex, and the H3K4me3 eraser, KDM5B. Our findings have thus uncovered a role of METTL14 in the regulation of bivalent domains and gene expression, independent of METTL3-mediated m^6A.

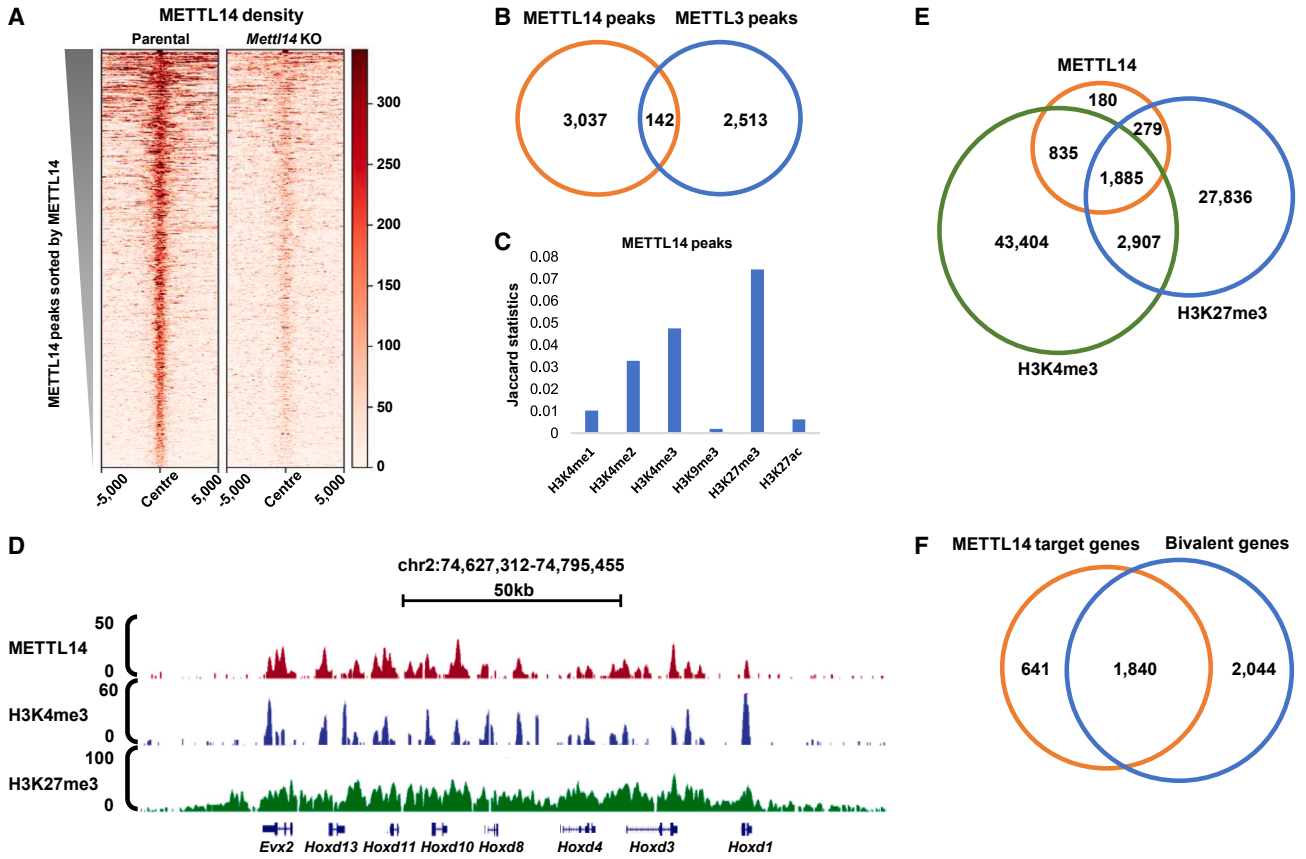

Figure 1. METTL14 binds to bivalent domains

(A) Heatmaps showing density of METTL14 on METTL14 peaks (n = 3,179) in parental and *Mettl14* KO cell lines.

(B) Venn diagram showing overlaps between METTL14 and METTL3 peaks. p = 1.24e−175. Fisher's exact test.

(C) Bar graph showing the overlapping rates (Jaccard statistics; see STAR Methods) of METTL14 peaks with peaks of different histone modifications.

(D) UCSC genome browser snapshots showing the binding patterns of METTL14 and histone modifications at representative bivalent domains.

(E) Venn diagram showing overlaps between METTL14 peaks and bivalent domains. p = 0. Fisher's exact test.

(F) Venn diagram showing overlaps between METTL14 target genes and bivalent genes. p = 0. Fisher's exact test.

Heatmaps were ranked according to METTL14 density in parental cells in descending order in (A). Two replicates of H3K4me3 and H3K27me3 ChIP-seq were performed.

RESULTS

METTL14 primarily binds to bivalent domains

We carried out chromatin immunoprecipitation sequencing (ChIP-seq) of METTL14 in mESCs and identified 3,179 METTL14-enriched peaks, which are significantly reduced in the *Mettl14* knockout (KO) cells (Figures 1A and S1A–S1C), suggesting that these peaks represent *bona fide* METTL14-binding sites. To further exclude ChIP-seq signals that might be caused by antibody cross-reactivities and to confirm our finding, we first generated mESCs in which the endogenous *Mettl14* alleles are tagged with FLAG-FKBP12^{F36V}. METTL14 proteins can be degraded rapidly (12 h) upon addition of degradation tag 13 (dTAG-13) (Figure S1D). We then carried out ChIP-seq with a FLAG antibody in this cell line in the presence and absence of dTAG-13, which induced METTL14 degradation (Figure S1E). As METTL14 forms heterodimers with METTL3,[28] we next determined METTL3 binding sites by analyzing public available ChIP-seq datasets.[16] Surprisingly, we found that, by and large, METTL14 does not co-localize with METTL3 on chromatin (4.5%, 142/3,179) no matter whether METTL14 locations are identified by METTL14 antibodies (Figure 1B) or by FLAG antibodies in the dTAG-METTL14 cell line (Figure S1F). Specifically, METTL14 is significantly enriched at gene promoters and CpG islands (39.4%, 1,252/3,179), while METTL3 is mostly localized to introns and intergenic regions (98%, 2,604/2,656) as reported previously,[16] suggesting that METTL14 may play a METTL3-independent role on chromatin.

To investigate potential roles of METTL14 on chromatin, we first investigated the histone modification features at its binding sites by analyzing the public ChIP-seq datasets in mESCs.[29] We observed substantial overlaps between METTL14 and H3K4me3 peaks (75.8%, 2,409/3,179), which are associated with active promoters but not with H3K27ac (14.7%, 466/3,179), which is another active promoter mark. METTL14 binding sites also substantially overlap with the repressive histone mark H3K27me3

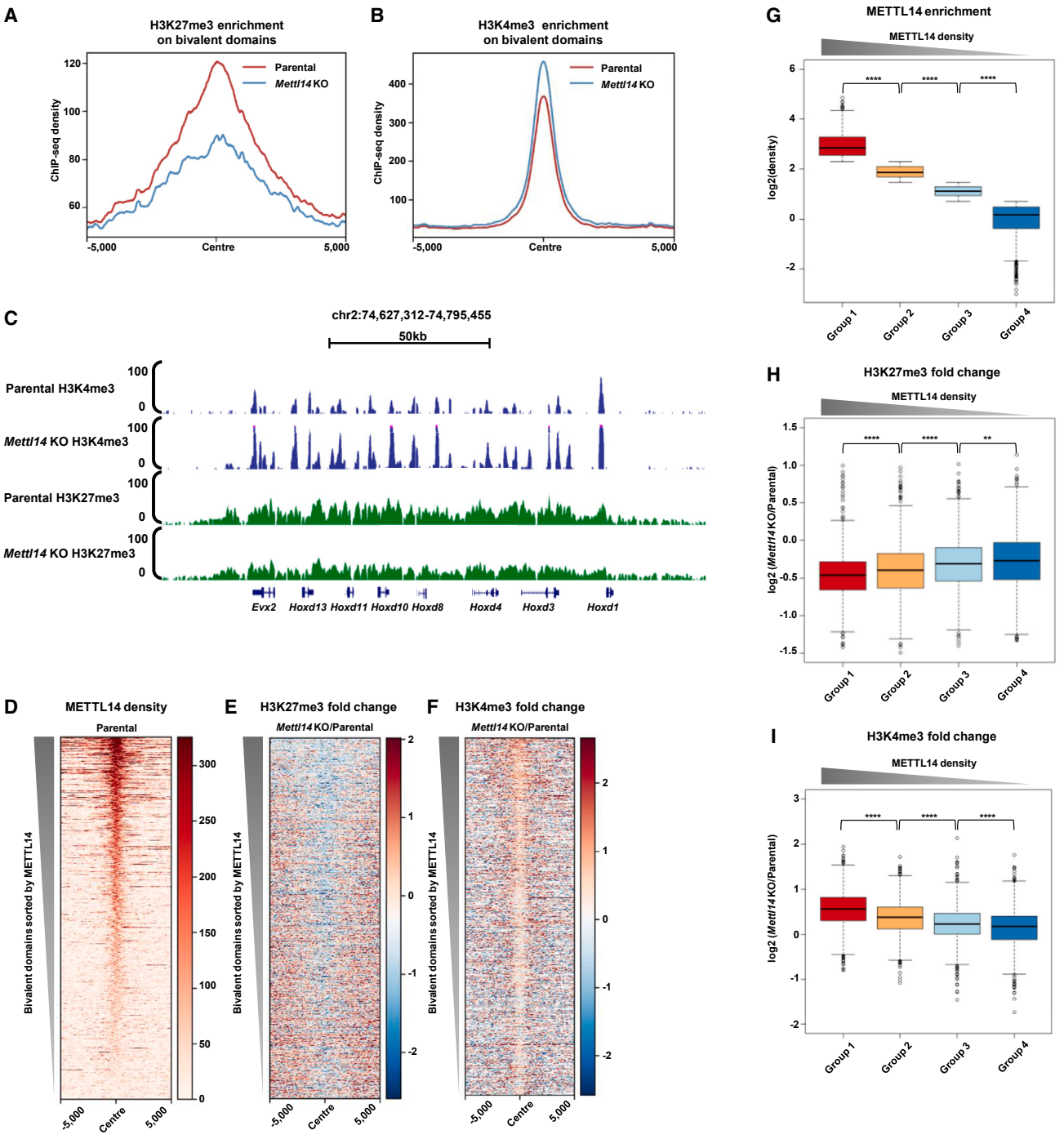

Figure 2. METTL14 regulates histone modifications at bivalent domains

(A and B) Aggregation plots showing the average enrichments of H3K27me3 (A) and H3K4me3 (B) at bivalent domains (n = 4,863) in parental and *Mettl14* KO cell lines.

(C) UCSC genome browser snapshots showing the binding patterns of histone modifications on representative bivalent domains in parental and *Mettl14* KO cell lines.

(D) Heatmap showing densities of METTL14 at bivalent domains (n = 4,863) in parental cell lines.

(E and F) Heatmaps showing ChIP-seq fold changes (log2(*Mettl14* KO/parental)) of H3K27me3 (E) and H3K4me3 (F) at bivalent domains (n = 4,863).

(G) Boxplot showing density (log2(density)) of METTL14 at bivalent domains quartered into four groups according to METTL14 binding density from high to low (n = 1,216, 1,216, 1,216, and 1,215 peaks in groups 1, 2, 3, and 4, respectively). ****$p < 0.0001$ (exact p values from left to right: 0, 0, and 0), two-sided paired t test.

(legend continued on next page)

(74.5%, 2,367/3,179). The Jaccard statistics (see STAR Methods) between METTL14 binding sites and histone modification peaks also show strong correlations of METTL14 with H3K4me3 and H3K27me3 (Figure 1C). Chromatin regions composed of both H3K4me3 and H3K27me3 are termed bivalent domains, which play crucial roles in regulating developmental genes during mouse embryo development.[2] Our findings thus suggest that METTL14 specifically binds to bivalent domains in mESCs. We further performed H3K4me3 and H3K27me3 ChIP-seqs and calculated co-enrichments of H3K4me3 and H3K27me3 with METTL14 (Figure 1D). Indeed, we found that a large proportion of METTL14 binding sites (59.3%, 1,885/3,179) overlapped with bivalent domains, while 26.2% (835/3,179) and 8.8% (279/3,179) overlapped with H3K4me3 only and H3K27me3 only, respectively (Figure 1E). In order to determine whether METTL14 binding sites harbor both H3K4me3 and H3K27me3 simultaneously, we carried out the ChomeID technique[30] to capture H3K4me3-H3K27me3 co-decorated chromatin regions. Specifically, we overexpressed a hemagglutinin (HA)-tag-fused protein containing a H3K27me3 reader domain (CBX7_Chromo) and a H3K4me3 reader domain (TAF3_Phd) in mESCs (Figure S1G) and performed HA ChIP. Consistent with previous study, we found that the HA ChIP enrichment level at bivalent regions is significantly higher than monovalent regions (Figure S1H). In addition, we found the fused protein is enriched at METTL14 binding sites (Figure S1I), supporting the idea that the METTL14 binding sites contain both H3K4me3 and H3K27me3. In addition, most of METTL14 target genes (74.2%, 1,840/2,480) are bivalent genes (Figure 1F), whose transcription is regulated by H3K4me3 and H3K27me3 at bivalent domains.[2] Collectively, these observations suggest that METTL14 specifically binds to bivalent domains and may play a regulatory role in mESCs.

METTL14 loss leads to decreased H3K27me3 and increased H3K4me3 levels at bivalent domains

To investigate the functional importance of METTL14 enrichment at bivalent domains, we first asked whether METTL14 regulates key histone modifications at bivalent domains by carrying out H3K4me3 and H3K27me3 ChIP-seq in parental and *Mettl14* KO cell lines. We identified an overall decrease of H3K27me3 as well as an overall increase of H3K4me3 at bivalent domains upon METTL14 loss (Figures 2A, 2B, and S2A), suggesting that METTL14 regulates bivalent domain integrity in mESCs. We further verified the change of H3K27me3 levels by ChIP-qPCR (Figure S2B). UCSC genome browser snapshots of H3K4me3 and H3K27me3 at a cluster of representative bivalent genes in parental and *Mettl14* KO cells are shown in Figures 2C and S2C, respectively. Importantly, we observed positive correlations between METTL14 binding density and fold changes of H3K27me3 and H3K4me3 (Figures 2D–2F). Specifically, we divided bivalent domains into four groups representing differential METTL14 binding intensities ranging from high to low (Figure 2G). We observed that bivalent domains with higher METTL14 binding showed a greater decrease of H3K27me3 as well as a greater increase of H3K4me3 upon METTL14 depletion (Figures 2H and 2I). These data suggest that METTL14 regulates both H3K27me3 and H3K4me3 at bivalent domains. As METTL14 depletion may lead to mESC differentiation, to reduce the bias caused by potential cell identity change, we also performed H3K4me3 and H3K27me3 ChIP-seq in the dTAG-METTL14 cells where METTL14 can be degraded rapidly before cells manifest signs of differentiation. Consistently, while no significant cell morphology change was observed (Figure S2D), the 24 h dTAG treatment caused a near-complete depletion of METTL14 (Figure S1E) and a prominent increase in H3K4me3 (Figure S2E). However, we observed only a very modest decrease of H3K27me3 (Figure S2F). We reasoned that it is possibly due to the relatively longer turnover rate of this modification and that more than 24 h is needed to observe significant changes. Alternatively, but not mutually exclusively, METTL14 may contribute to the *de novo* establishment of H3K27me3. To test this possibility, we treated the mESCs with the PRC2 inhibitor EPZ6438 for 7 days. We then withdrew EPZ6438 and treated the cells with DMSO or dTAG-13 for an additional 24 h before measuring the H3K27me3 level. We found that the H3K27me3 level was decreased to the background level after EPZ6438 treatment and restored after EPZ6438 withdrawal (Figure S2G). It is worth noting that the restored H3K27me3 level is significantly lower in the METTL14 depleted cells, suggesting that METTL14 plays an important role in H3K27me3 establishment (Figure S2G).

METTL14 loss leads to increased transcription of bivalent genes

As the transcription activity of bivalent genes is regulated by the balance between the active mark H3K4me3 and the repressive mark H3K27me3,[2] we next asked whether the RNA level of bivalent genes is impacted by METTL14 depletion. We performed RNA-seq in parental and *Mettl14* KO cells and found significantly increased expression of METTL14-bound bivalent genes (Figure 3A). On the contrary, such an increase is not observed in the METTL14-unbound bivalent genes or the METTL14-bound non-bivalent genes (Figure 3A). We further showed that bivalent genes with higher METTL14 binding showed a greater increase of their expression levels (Figure 3B). qRT-PCR assays also validated that *Mettl14* KO led to an increase of the expression levels of METTL14-bound bivalent genes (i.e., the *Hoxd* family genes,

(H and I) Boxplot showing ChIP-seq fold changes (log2(*Mettl14* KO/parental)) of H3K27me3 (H) and H3K4me3 (I) on four groups of bivalent domains as in (G). $^{**}p < 0.01$, $^{****}p < 0.0001$ (exact p values of H from left to right: 2.34e−06, 2.12e−09, and 8.60e−03; exact p values of I from left to right: 3.45e−30, 1.52e−16, and 1.19e−07), two-sided t test.

For boxplots in (G)–(I), the middle line and lower and upper hinges of the boxplot correspond to the median and the first and third quartiles, respectively. The whiskers extend from the hinges to no further than 1.5× IQR (interquartile range) from the hinge. Outlying points are plotted individually. Heatmaps were ranked according to METTL14 density in parental cells in descending order in (D)–(F). For boxplots in (D)–(F), the middle line and lower and upper hinges of the boxplot correspond to the median and the first and third quartiles, respectively. The whiskers extend from the hinges to no further than 1.5× IQR from the hinge. Outlying points are plotted individually. ChIP-seq density is added by 1 before log2 transformation.

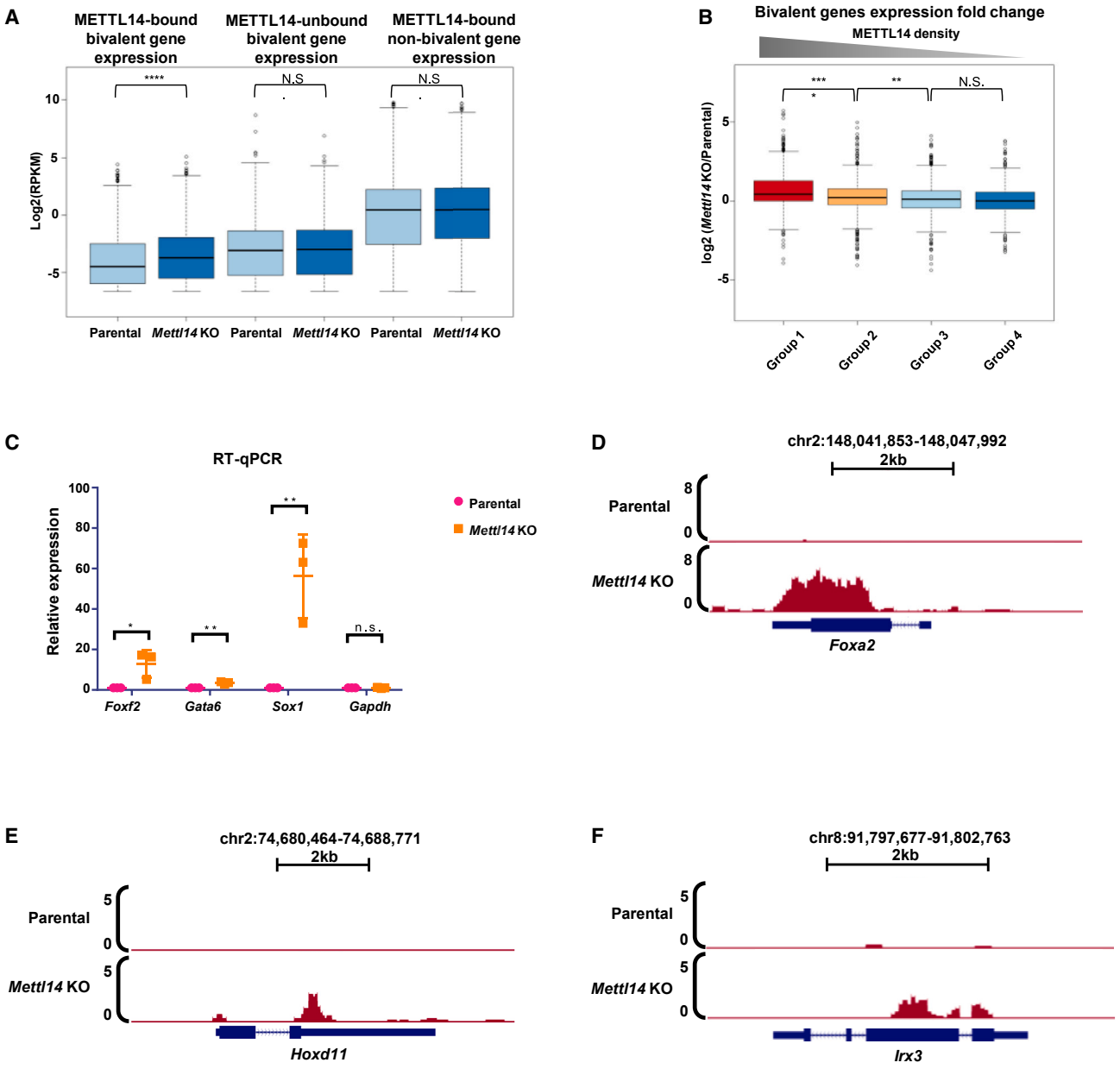

Figure 3. METTL14 regulates transcription of bivalent genes

(A) Boxplot showing RNA-seq densities (log2(RPKM)) of the METTL14-bound bivalent genes (n = 1,840), METTL14-unbound bivalent genes (n = 2,044), and other METTL14-bound genes (n = 641) in parental and *Mettl14* KO cell lines. ****p < 0.0001 (exact p values from left to right: 8.08–10, 3.35e–01, and 5.09e–01), two-sided t test.

(B) Boxplot showing RNA-seq densities fold changes (log2(*Mettl14* KO/parental)) of the bivalent genes associated with the four groups of bivalent domains defined in Figure 2G (n = 1,087, 1,035, 973, and 789 genes in groups 1, 2, 3, and 4, respectively). **p < 0.01, ****p < 0.0001 (exact p values from left to right: 2.19e–14, 5.14e–03, and 3.25e–01), two-sided t test.

(C) qRT-PCR showing relative expression levels of bivalent genes (*Foxa2*, *Irx3*, *Hoxd11*) in parental and *Mettl14* KO cell lines. The mean of three biological replicates ± SD is shown. *p < 0.05, **p < 0.01 (exact p values from left to right: 3.69e–02, 2.50e–03, 9.81e–03, and 9.70e–01), two-sided t test.

(D–F) UCSC genome browser snapshots showing the transcription levels of bivalent genes (*Foxa2*, *Irx3*, *Hoxd11*) in parental and *Mettl14* KO cell lines.

For boxplots in (A) and (B), the middle line and lower and upper hinges of the boxplot correspond to the median and the first and third quartiles, respectively. The whiskers extend from the hinges to no further than 1.5× IQR from the hinge. Outlying points are plotted individually. RNA-seq density is added by 0.01 before log2 transformation. Two replicates of RNA-seq were performed. Three replicates of H3K27me3 ChIP-qPCR were performed.

Foxf2, *Irx3*) (Figure 3C). Such alterations were shown in UCSC genome browser snapshots (Figures 3D–3F). In addition, we showed that protein levels of these genes are also up-regulated in *Mettl14* KO cells (Figure S3A). Gene Ontology (GO) analysis revealed that bivalent genes regulated by METTL14 were closely associated with multicellular organism development (Figure S3B), consistent with the report that METTL14 is important for development and differentiation.[31] Collectively, these findings suggest that METTL14 binds and regulates bivalent gene expression in mESCs.

METTL3 is not required for METTL14 to regulate bivalent domains

METTL3 and METTL14 form a stable heterodimer mRNA m^6A methyltransferase complex.[28] To explore whether m^6A was involved in METTL14-mediated regulation of bivalent domains, we generated and validated rescued cell lines containing either wild-type METTL14 ($METTL14^{WT}$) or mutants unable to support METTL3-mediated m^6A methylation ($METTL14^{R298A}$ and $METTL14^{D312A}$)[23] (Figures S3C and SD). Interestingly, we found that $METTL14^{WT}$ and mutants ($METTL14^{R298A}$ and $METTL14^{D312A}$) both readily restored H3K27me3 and H3K4me3 in the *Metttl4* KO cells (Figures 4A, 4B, and S3E–S3F). Consistently, bivalent domains with higher METTL14 binding showed a greater decrease of H3K27me3 as well as a greater increase of H3K4me3 upon METTL14 depletion, which can be rescued by $METTL14^{WT}$ as well as by $METTL14^{R298A}$ and $METTL14^{D312A}$ (Figures 4C and 4D).

In order to further investigate whether m^6A catalytic activity impacts bivalent chromatin, we carried out H3K27me3 and H3K4me3 ChIP-seq in parental and *Mettl3* KO cell lines. We found no overt changes of H3K4me3 in response to METTL3 loss (Figure S3G). However, the H3K27me3 level is significantly down-regulated. Since METTL3 is barely detectable at bivalent domains (Figures 1B and S3H), this reduction of H3K27me3 is likely due to an indirect effect of METTL3.

These results, coupled with the distinct genomic locations of METTL3 and METTL14 in mESCs, suggest that METTL3 and m^6A are not required for METTL14 to regulate histone modifications at bivalent domains.

Since METTL14 is an RBP and works with METTL3 to deposit m^6A co-transcriptionally, we next asked whether METTL14 binding to chromatin is regulated by transcription. We performed FLAG ChIP in the dTAG-METTL14 cells treated with the transcription inhibitor triptolide and found no significant changes of FLAG-METTL14 binding upon triptolide treatment (Figure S3I), suggesting that METTL14 binding to bivalent domains is likely to be independent of transcription.

METTL14 interacts with H3K4me3 methyltransferase complex PRC2 and the H3K4me3 demethylases KDM5A and KDM5B

To gain mechanistic insight into the METTL14 function at bivalent domains, we next set out to identify METTL14-interacting proteins under conditions where METTL3 is absent by purifying an HA-tagged METTL14 and its associated proteins from the nucleus of *Mettl3* KO mESCs (Figure S4A; Table S1). GO analysis of the co-immunoprecipitated proteins showed that METTL14-interacting proteins were enriched in mRNA-associated and chromatin-associated pathways (Figure S4B). Specifically, among the high-confident candidates, we found EED and SUZ12, which are core subunits of the H3K27me3 methyltransferase PRC2 complex, as well as KDM5A and KDM5B, which are H3K4me3 demethylases (Figure S4C). We validated the interactions between the endogenous METTL14 and the PRC2 complex and KDM5A/5B in mESCs by reciprocal co-immunoprecipitation (Figures 5A and 5B). Furthermore, *in vitro* pull-down experiments suggested that METTL14 may directly interact with PRC2 and KDM5A/5B (Figures 5C and 5D). In order to map the regions of METTL14 that interact with the PRC2 complex, we overexpressed different truncations of METTL14 (Figure S4D) and confirmed that the C-terminal region of METTL14 was important for the METTL14-PRC2 interaction (Figure S4E), which is consistent with the previous report that the C-terminal region of METTL14 is essential for the interaction between METTL14 and other proteins.[32]

METTL14 co-localizes with PRC2 and KDM5B and is required for PRC2 binding at bivalent domains

The interactions between METTL14 and the PRC2 complex and KDM5A/5B raised an interesting possibility that METTL14 may regulate bivalent domains by collaborating with these critical enzymes relevant to bivalency regulation. We first asked whether METTL14 co-binds with these proteins on chromatin. EZH2, EED, and SUZ12 ChIP-seqs identified 3,570, 3,201, and 3,839 binding sites at bivalent domains, respectively, which we further found to be significantly overlapped with METTL14 binding sites (Figure 5E). Consistently, we found that bivalent domains are enriched for EZH2, EED, and SUZ12 (Figures 5F and S5A–S5C), and their binding densities on these elements were positively correlated with METTL14 (Figures S5D–S5F), suggesting that METTL14 co-occupies with PRC2 at these regions.

Because of the lack of commercially available ChIP-grade antibodies for KDM5A/5B, we next interrogated KDM5A/5B chromatin localizations by analyzing public ChIP-seq datasets in mESCs[33,34] and identified 2,626 KDM5A and 7,921 KDM5B binding sites, respectively (Figures 5G and 5H). We found overlaps of a large proportion of METTL14 binding sites with KDM5B (30.2%, 961/3,179) but not KDM5A (1.57%, 50/3,179) (Figures 5G and 5H). Consistently, we found that the binding density of KDM5B, but not KDM5A, at bivalent domains correlated positively with that of METTL14 (Figures 5I, 5J, and S5G–S5H), suggesting that METTL14 might regulate chromatin binding of KDM5B but not KDM5A. Importantly, the binding densities of EZH2, EED, and SUZ12 at bivalent domains were reduced in the *Mettl14* KO cells, while the overall protein levels of EZH2, EED, and SUZ12 were largely unaltered in the *Mettl14* KO cells (Figures 6A–6C and S5I–S5L). We confirmed the decrease of EED binding at several representative loci by ChIP-qPCR (Figure S5M). In addition, bivalent domains with higher METTL14 binding also showed a greater decrease of PRC2 complex occupancy in the *Mettl14* KO cells (Figures 6D–6F), suggesting that METTL14 specifically regulates PRC2 binding at bivalent domains. Consistent with this METTL14-PRC2 regulation axis, we showed that PCR2 loss led to a similar up-regulation of bivalent genes as did the METTL14 loss by reanalyzing the published

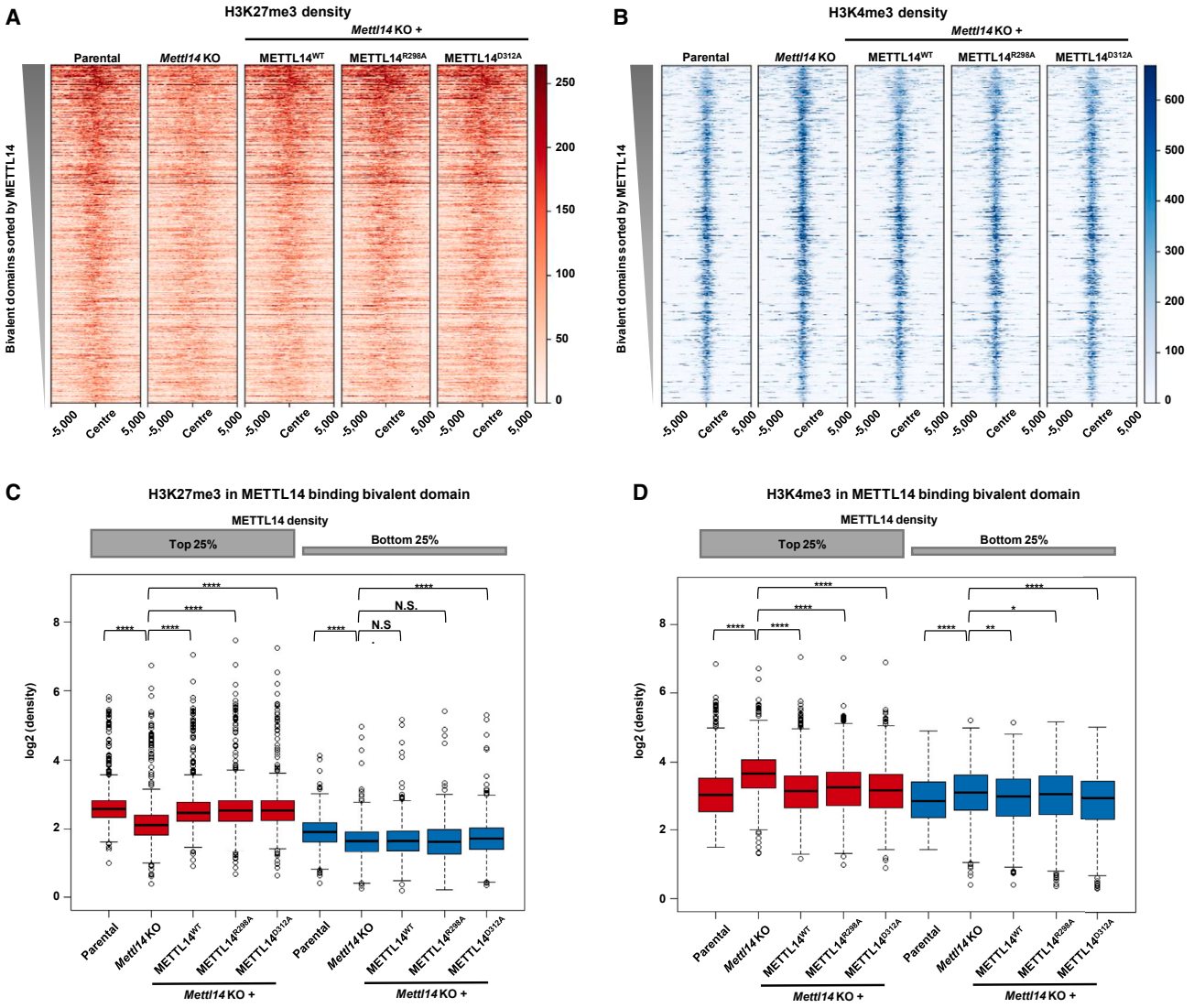

Figure 4. METTL14 regulating at bivalent domains is independent of m^{6}A

(A and B) Heatmaps showing densities of H3K27me3 (A) and H3K4me3 (B) at bivalent domains (n = 4,863) in parental, *Mettl14* KO, and rescued cell lines with METTL14^{WT}, METTL14^{R298A}, or METTL14^{D312A}.

(C and D) Boxplots showing densities (log2(density)) of H3K27me3 (C) and H3K4me3 (D) on groups 1 and 4 of bivalent domains as in Figure 2G in parental, *Mettl14* KO, and rescued cell lines with METTL14^{WT}, METTL14^{R298A}, or METTL14^{D312A}. *p < 0.05, **p < 0.01,****p < 0.0001 (exact p values of C from left to right: 1.38e–80, 5.18e–52, 1.14e–56, 3.78e–58, 1.08e–44, 1.22e–01, 6.66e–01, and 1.68e–05; exact p values of D from left to right: 1.67e–78, 2.75e–64, 4.01e–44, 3.61e–61, 1.04e–06, 1.92e–04, 1.28e–02, and 8.82e–10), two-sided t test.

Heatmaps were ranked according to METTL14 density in parental cells in descending order in (A) and (B). For boxplots in (C) and (D), the middle line and lower and upper hinges of the boxplot correspond to the median and the first and third quartiles, respectively. The whiskers extend from the hinges to no further than 1.5× IQR from the hinge. Outlying points are plotted individually. ChIP-seq density is added by 1 before log2 transformation/two replicates of H3K4me3 and H3K27me3 ChIP-seq were performed.

RNA-seq data (GEO: GSE56312 and GSE136584) (Figures S6A and S6B).[35,36]

Due to the lack of a commercially available ChIP-grade antibody, we were not able to investigate the endogenous KDM5B binding profile in the *Mettl14* KO mESCs. In order to overcome this obstacle, we knocked in the FLAG tag at the N terminus of the endogenous *Kdm5b* gene in parental and *Mettl14* KO cells (Figure S6C) and performed FLAG ChIP. Consistent with the up-regulated H3K4me3 level at bivalent regions, we showed that the binding densities of FLAG-KDM5B are significantly down-regulated upon METTL14 loss (Figure S6D).

In summary, our findings identified an important function of METTL14 in bivalent domain regulation independent of METTL3 and m^{6}A modification in mESCs and revealed a potential underlying mechanism, thus providing important insight into mechanisms of bivalent domain regulation in mammals.

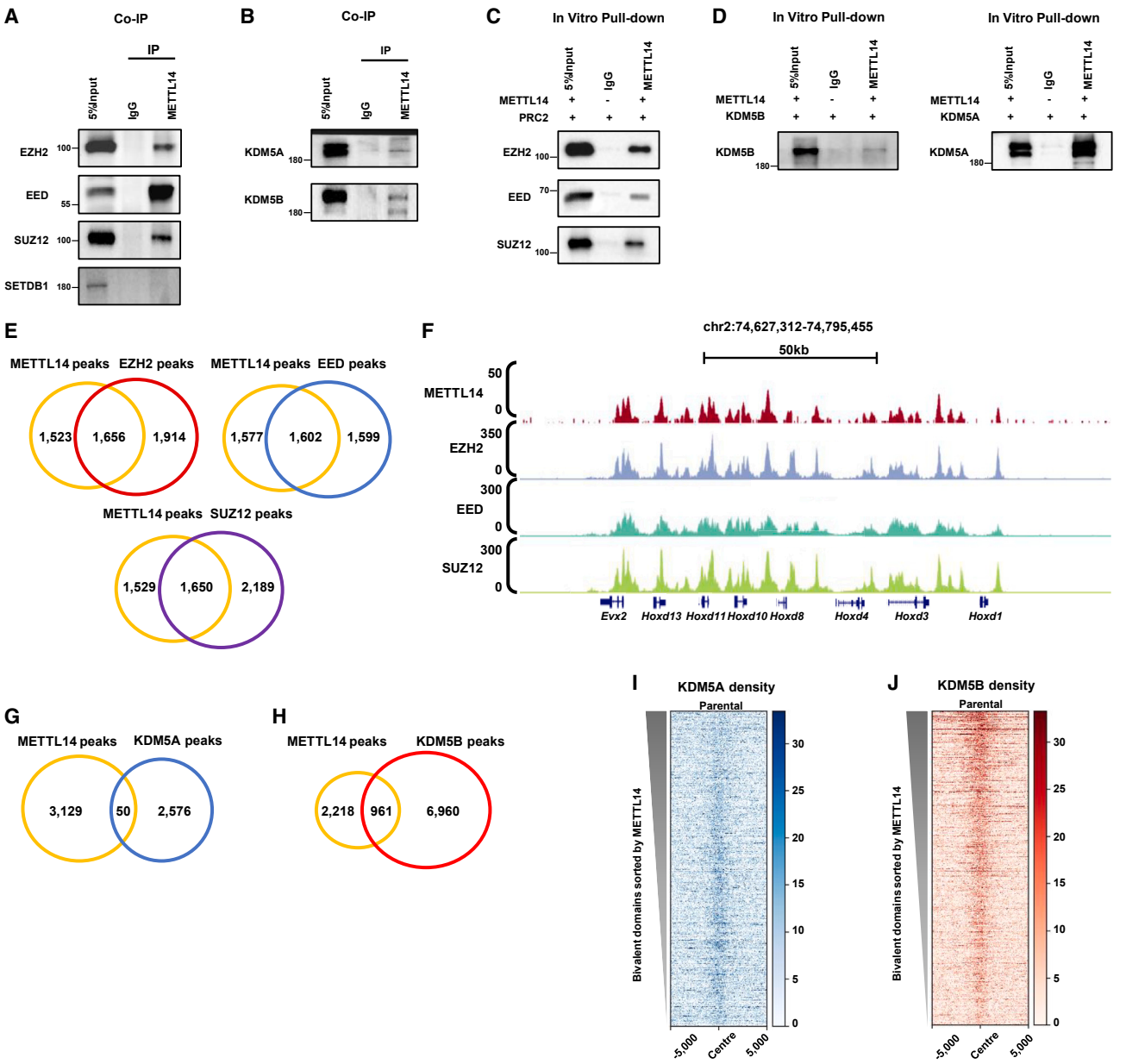

Figure 5. PRC2 and KDM5A/5B localizations are correlated with METTL14 at bivalent domains

(A) Western blots showing reciprocal immunoprecipitation of METTL14 and PRC2 complex (EZH2, EED, SUZ12).

(B) Western blots showing reciprocal immunoprecipitation of METTL14 and KDM5A/KDM5B.

(C) Western blots showing *in vitro* pull-down of METTL14 and PRC2 complex (EZH2, EED, SUZ12).

(D) Western blots showing *in vitro* pull-down of METTL14 and KDM5A (left) and KDM5B (right).

(E) Venn diagram showing overlaps between METTL14 and EZH2 and EED and SUZ12 (exact p values from left to right: 0, 0, and 0). Fisher's exact test.

(F) UCSC genome browser snapshots showing densities of METTL14, EZH2, EED, and SUZ12 at bivalent domains in parental cell line.

(G and H) Venn diagram analysis showing overlaps between METTL14 and KDM5A (G) and KDM5B (H) (exact p value of G: 8.07e–41; exact p value of H: 0), Fisher's exact test.

(I–J) Heatmaps showing densities of KDM5A (I) and KDM5B (J) at bivalent domains (n = 4,863) in parental cell line.

For blots, representative of two independent experiments are shown in (A)–(D). Heatmaps were ranked according to METTL14 density in parental cells in descending order in (I) and (J). ChIP-seq density is added by 1 before log2 transformation. Two replicates of EZH2, EED, and SUZ12 ChIP-seq were performed.

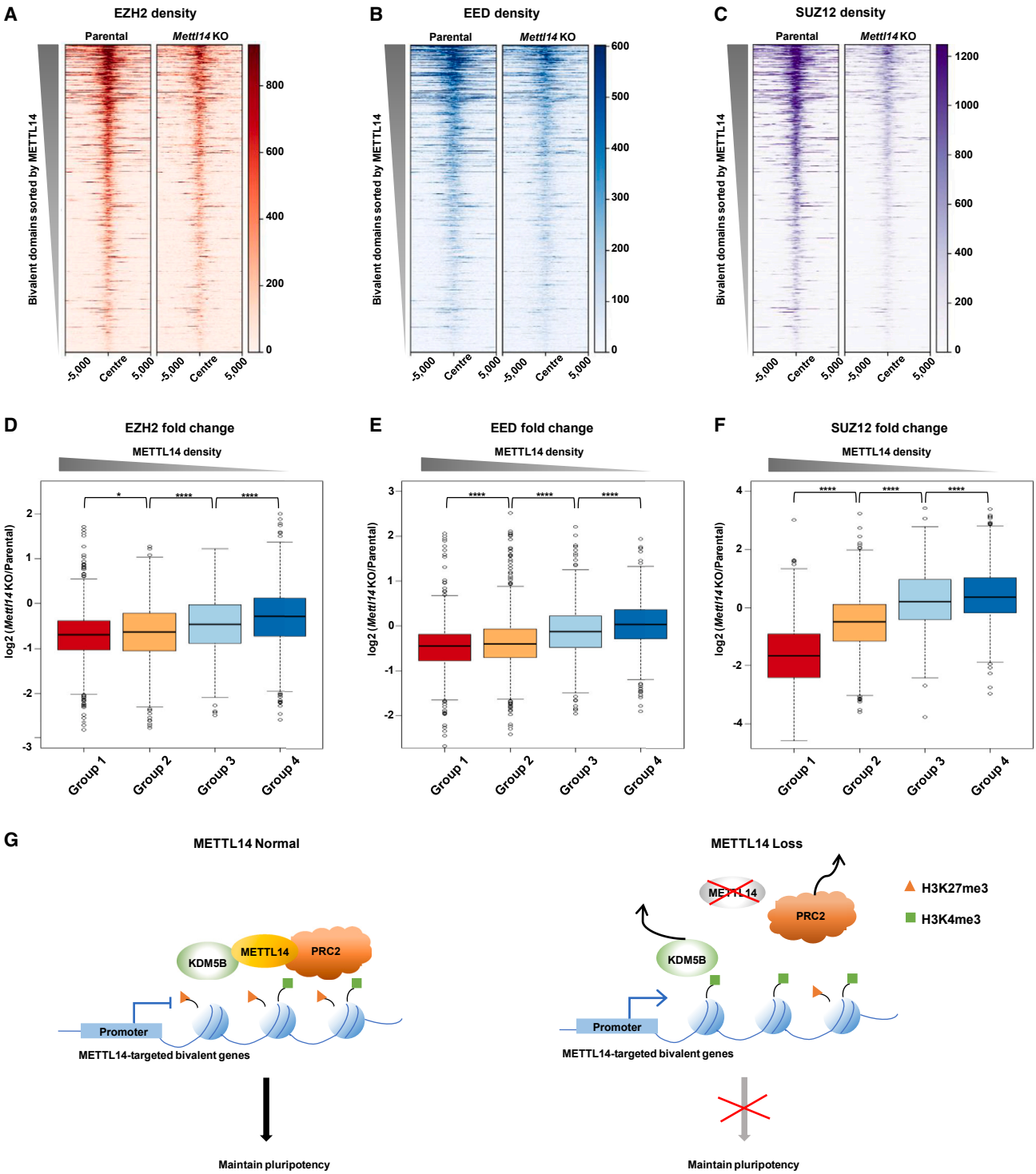

Figure 6. METTL14 regulates PRC2 localization to bivalent domains

(A–C) Heatmaps showing densities of EZH2 (A), EED (B), and SUZ12 (C) at bivalent domains (n = 4,863) in parental and *Mettl14* KO cell lines.

(D–F) Boxplot showing ChIP-seq fold changes (log2(*Mettl14* KO/parental)) of EZH2 (D), EED (E), and SUZ12 (F) on four groups of bivalent domains as in Figure 2G. *p < 0.05, ****p < 0.0001 (exact p values of D from left to right: 1.71e–02, 3.50e–13, 5.34e–08; exact p values of E from left to right: 3.74e–07, 3.04e–27, and 1.80e–12; exact p values of F from left to right: 7.19e–145, 1.79e–71, and 6.19e–06), two-sided t test.

(G) Schematic model showing METTL14 regulates PRC2 and KDM5B localization at bivalent domains. Loss of METTL14 results in a decrease of H3K27me3 and an increase of H3K4me3 and the subsequent activation of these METTL14-bound bivalent genes.

(legend continued on next page)

DISCUSSION

In this study, we revealed a chromatin binding profile of METTL14 and provided evidence that METTL14 regulates bivalent domain integrity in mESCs. Our conclusion is supported by multiple lines of evidence including the demonstrations that (1) METTL3 is not required for METTL14 to regulate bivalent domains; (2) METTL14 co-localizes with PRC2 and is required for PRC2 enrichment to deposit H3K27me3 at bivalent domains; (3) METTL14 also interacts with KDM5B, which is required for H3K4me3 regulation at bivalent domains; and (4) chromatin-bound METTL14 is important for transcription activity of bivalent genes, as loss of METTL14 increases transcription of those bivalent genes bound by METTL14 (Figure 6G). Importantly, our findings have uncovered a unique role of METTL14 in the bivalent domain regulation independent of METTL3-mediated m^6A.

Our findings show that the presence of PRC2 and KDM5B at bivalent domains is regulated by METTL14, as loss of METTL14 leads to a significant reduction of these enzymes at bivalent sites, suggesting that METTL14 could play a role in the binding of these enzymes at bivalent domains to ensure the integrity of bivalent domains. Our finding that METTL14 physically interacts with PRC2 and KDM5B suggests that METTL14 accomplishes this function by regulating H3K27me3 and H3K4me3 through interactions with PRC2 and KDM5B. However, many questions remain unknown. For instance, how is METTL14 specifically recruited to bivalent domains to begin with? Given that METTL14 can bind RNA, chromatin-associated RNAs, including nascent transcripts and long non-coding RNAs (lncRNAs),[37] might contribute to METTL14 binding, either through direct interactions or indirect interactions mediated by other RBPs such as NONO and PSPC1, which are known regulators of bivalent domains.[8,9] Interestingly, a recent study showed that METTL14 specifically binds to G-quadruplex RNAs through its RGG domain,[38] suggesting that RNAs with specific secondary structures might regulate METTL14 binding. Interestingly, DNAs at bivalent domains have also been shown to preferentially form G-quadruplexes,[39,40] and thus it will be of great interest to explore whether DNA or RNA secondary structures impact METTL14 binding to bivalent domains. Additionally, METTL14 has also been shown to bind H3K36me3.[41] Although this modification is not enriched at bivalent domains, the histone modifications that form the bivalent domains, i.e., histone H3K4me3 and H3K27me3, might also regulate METTL14 binding through direct or indirect interactions.

During the revision of this article, another study reported that METTL14 binds to H3K27me3-enriched chromatin regions.[42] Furthermore, they showed that H3K27me3 is up-regulated upon METTL14 loss. Since the *Mettl14* conditional KO (CKO) cell used in their study showed significant morphological changes, it remains unclear whether the change of H3K27me3 is a direct or secondary effect of METTL14 loss. In our study, we utilized a METTL14 acute depletion system to show that H3K27me3 is down-regulated within 24 h upon METTL14 loss, at which time point no obvious morphological changes were observed (Figure S2D). Mechanistically, their study showed that METTL14 interacts with H3K27me3 demethylase KDM6B to down-regulate H3K27me3 levels at bivalent domains. In our study, we found that the H3K27me3 level is mainly regulated by METTL14 physically interacting and probably recruiting the PRC2 complex and that, consistently, METTL14 loss significantly impaired the binding densities of PRC2 components at bivalent domains. Taken together, our data suggest that METTL14 directly promotes PRC2 binding and enhances H3K27me3 levels at bivalent domains, though our data do not rule out the possibility that METTL14 may also regulates H3K27me3 levels via KDM6B as well. The exact mechanism of METTL14 regulating H3K27me3 may be complex and different in different cell types and under different conditions and therefore needs further investigation.

Another question that remains unanswered is the impact of elevated H3K4me3 upon METTL14 depletion. Recent studies suggested that H3K4me3 is not required for the activation of bivalent genes[6] but is crucial for keeping these genes from DNA methylation, which induces permanent gene silencing.[5,6] It will be of great interest to investigate in the future whether the up-regulated H3K4me3 in *Mettl14* KO cells leads to DNA methylation changes during embryo development.

Taken together, our data show that METTL14 is enriched at bivalent domains, similar to that of the PRC2 complex and the H3K4me3-specific demethylase KDM5B. Our data further suggest that METTL14 regulates PRC2 and KDM5B localization to bivalent domains, possibly through protein-protein interactions. As a result, loss of METTL14 leads to the reduction of H3K27me3 and subsequent activation of these bivalent genes. Our findings uncovered a mechanism that regulates bivalent domains and a unique role of METTL14, independent of METTL3-mediated m^6A, which may contribute to embryo development.

Limitations of the study

We carried out ChIP-seq of METTL14 with endogenous METTL14 antibody in mESCs and identified 3,179 METTL14-enriched peaks. To further exclude ChIP-seq signals that might be caused by antibody cross-reactivities, we also generated mESCs in which the endogenous *Mettl14* alleles were tagged with FLAG-$FKBP12^{F36V}$ and carried out ChIP-seq with a FLAG antibody and found the endogenous METTL14 ChIP-seq peaks significantly overlap with the FLAG ChIP-seq signals (44.3%, 1,409/3,179).

We assessed the morphology change of mESCs to evaluate the potential impact of METTL14 loss on pluripotency/differentiation of the cells. We showed that the morphology of the cells seems to be flatter and less compact for the *Mettl14* KO cells (Figure S6E), suggesting signs of cell identity change. To mitigate

For boxplots in (D) and (E), the middle line and lower and upper hinges of the boxplot correspond to the median and the first and third quartiles, respectively. The whiskers extend from the hinges to no further than 1.5× IQR from the hinge. Outlying points are plotted individually. Heatmaps were ranked according to METTL14 density in parental cells in descending order in (A)–(C). ChIP-seq density is added by 1 before log2 transformation. Two replicates of EZH2, EED, and SUZ12 ChIP-seq were performed.

this issue, we utilized dTAG technology by integrating the FLAG-FKBP12^{F36V} tag at the N terminus of the endogenous *Mettl14* locus. The addition of dTAG-13 induced a rapid depletion of METTL14 proteins (Figure S1D), but we observed no significant morphology change at 24 h after dTAG-13 treatment (Figure S2D), which is the time point at which we carried out ChIP-seq experiments. In addition, H3K27me3 levels are significantly higher in METTL14^{WT}, METTL14^{R298A}, or METTL14^{D312A} rescued cells than *Mettl14* KO cells, while only METTL14^{WT}, but not METTL14^{R298A} or METTL14^{D312A}, rescued cells show a significant difference in cell morphology (Figure S6E), suggesting that the m^{6}A-related function of METTL14 impacts stem cell identity but that regulation of H3K27me3 is independent of the m^{6}A-related function of METTL14. It would be helpful to do METTL14 ChIP in the *Mettl14* KO and METTL14^{WT}, METTL14^{R298A}, or METTL14^{D312A} rescued cells to match the H3K27me3 and H3K4me3 data in Figures 4A and 4B. Unfortunately, we could not perform METTL14 ChIP in the rescued cells because the ChIP-grade METTL14 antibody was no longer available at that time. Additional insights into the regulation of H3K27me3 by METTL14 need further studies, such as investigating whether artificially tethering METTL14^{WT}, METTL14^{R298A}, or METTL14^{D312A} by a CRISPR-based technology can restore H3K27me3 at bivalent regions.

STAR★METHODS

Detailed methods are provided in the online version of this paper and include the following:

- KEY RESOURCES TABLE
- RESOURCE AVAILABILITY
  - Lead contact
  - Materials availability
  - Data and code availability
- EXPERIMENTAL MODEL AND STUDY PARTICIPANT DETAILS
  - Cell culture
- METHOD DETAILS
  - Construction of stable cell lines and knockdown
  - TAP purification of METTL14 protein complex
  - Co-immunoprecipitation
  - Genome editing for dTAG endogenous knock-in
  - In vitro pull-down
  - Isolation of mRNA for QQQ and HPLC analysis
  - ChIP-seq
  - RT-qPCR
  - Western blots
  - Strand specific total RNA-seq
- QUANTIFICATION AND STATISTICAL ANALYSIS
  - ChIP-seq analysis
  - Total RNA-seq analysis
  - Analyses of repeats correlation

SUPPLEMENTAL INFORMATION

Supplemental information can be found online at https://doi.org/10.1016/j.celrep.2023.112650.

ACKNOWLEDGMENTS

H.S. was sponsored by the National Key R&D Program of China (2021YFA1102200 and 2021YFA1301700), the National Science Foundation of China (32122020 and 32070649), and the Science and Technology Commission of Shanghai Municipality (22TQ012). W.X. was sponsored by the Shanghai Rising-Star Program (22QA1402000) and the National Science Foundation of China (32270616). Y.S. is an American Cancer Society Research Professor.

AUTHOR CONTRIBUTIONS

M.M. and H.S. carried out the experiments. M.M. and W.X. carried out the bioinformatics analyses. X.L., Y.H., and L.Z. provided help on liquid chromatography tandem mass spectrometry (LC-MS/MS) analysis of m^{6}A. D.W. and Q.C. were involved in the identification of METTL14 KI cells. J.W., D.Z., and S.C. provided help with preparing the various METTL14 truncation constructs. L.D. and L.T. provided discussions and advice on mESC culture. P.Z. and F.W. provided discussion and advice on bioinformatics analyses. W.X., H.S., and Y.S. conceived the project and directed all the experiments with input from Y.G.S. and co-wrote the manuscript with M.M.

DECLARATION OF INTERESTS

Y.S. is a co-founder and member of the Scientific Advisory Broad of K36 Therapeutics and ABio, Inc. Y.S. is also a member of the scientific advisory board of Epicrispr Biotechnologies, Inc., and a member of the MD Anderson External Advisory Board. Y.S. holds equity in Active Motif, K36 Therapeutics, ABio, Inc., and Epicrispr Biotechnologies, Inc.

Received: July 13, 2022
Revised: April 11, 2023
Accepted: May 30, 2023
Published: June 13, 2023; corrected online September 4, 2023

REFERENCES

1. Liu, X., Wang, C., Liu, W., Li, J., Li, C., Kou, X., Chen, J., Zhao, Y., Gao, H., Wang, H., et al. (2016). Distinct features of H3K4me3 and H3K27me3 chromatin domains in pre-implantation embryos. Nature *537*, 558–562. https://doi.org/10.1038/nature19362.
2. Bernstein, B.E., Mikkelsen, T.S., Xie, X., Kamal, M., Huebert, D.J., Cuff, J., Fry, B., Meissner, A., Wernig, M., Plath, K., et al. (2006). A bivalent chromatin structure marks key developmental genes in embryonic stem cells. Cell *125*, 315–326. https://doi.org/10.1016/j.cell.2006.02.041.
3. Jadhav, U., Nalapareddy, K., Saxena, M., O'Neill, N.K., Pinello, L., Yuan, G.C., Orkin, S.H., and Shivdasani, R.A. (2016). Acquired tissue-specific promoter bivalency is a basis for PRC2 necessity in adult cells. Cell *165*, 1389–1400. https://doi.org/10.1016/j.cell.2016.04.031.
4. Zhang, J., Zhang, Y., You, Q., Huang, C., Zhang, T., Wang, M., Zhang, T., Yang, X., Xiong, J., Li, Y., et al. (2022). Highly enriched BEND3 prevents the premature activation of bivalent genes during differentiation. Science *375*, 1053–1058. https://doi.org/10.1126/science.abm0730.
5. Kumar, D., Cinghu, S., Oldfield, A.J., Yang, P., and Jothi, R. (2021). Decoding the function of bivalent chromatin in development and cancer. Genome Res. *31*, 2170–2184. https://doi.org/10.1101/gr.275736.121.
6. Douillet, D., Sze, C.C., Ryan, C., Piunti, A., Shah, A.P., Ugarenko, M., Marshall, S.A., Rendleman, E.J., Zha, D., Helmin, K.A., et al. (2020). Uncoupling histone H3K4 trimethylation from developmental gene expression via an equilibrium of COMPASS, Polycomb and DNA methylation. Nat. Genet. *52*, 615–625. https://doi.org/10.1038/s41588-020-0618-1.
7. Xiao, R., Chen, J.Y., Liang, Z., Luo, D., Chen, G., Lu, Z.J., Chen, Y., Zhou, B., Li, H., Du, X., et al. (2019). Pervasive chromatin-RNA binding protein interactions enable RNA-based regulation of transcription. Cell *178*, 107–121.e18. https://doi.org/10.1016/j.cell.2019.06.001.

8. Ma, C., Karwacki-Neisius, V., Tang, H., Li, W., Shi, Z., Hu, H., Xu, W., Wang, Z., Kong, L., Lv, R., et al. (2016). Nono, a bivalent domain factor, regulates erk signaling and mouse embryonic stem cell pluripotency. Cell Rep. *17*, 997–1007. https://doi.org/10.1016/j.celrep.2016.09.078.

9. Huang, X., Bashkenova, N., Hong, Y., Lyu, C., Guallar, D., Hu, Z., Malik, V., Li, D., Wang, H., Shen, X., et al. (2022). A TET1-PSPC1-Neat1 molecular axis modulates PRC2 functions in controlling stem cell bivalency. Cell Rep. *39*, 110928. https://doi.org/10.1016/j.celrep.2022.110928.

10. Xu, W., He, C., Kaye, E.G., Li, J., Mu, M., Nelson, G.M., Dong, L., Wang, J., Wu, F., Shi, Y.G., et al. (2022). Dynamic control of chromatin-associated m(6)A methylation regulates nascent RNA synthesis. Mol. Cell. *82*, 1156–1168.e7. https://doi.org/10.1016/j.molcel.2022.02.006.

11. Lee, J.H., Wang, R., Xiong, F., Krakowiak, J., Liao, Z., Nguyen, P.T., Moroz-Omori, E.V., Shao, J., Zhu, X., Bolt, M.J., et al. (2021). Enhancer RNA m6A methylation facilitates transcriptional condensate formation and gene activation. Mol. Cell. *81*, 3368–3385.e9. https://doi.org/10.1016/j.molcel.2021.07.024.

12. Liu, J., Dou, X., Chen, C., Chen, C., Liu, C., Xu, M.M., Zhao, S., Shen, B., Gao, Y., Han, D., and He, C. (2020). N (6)-methyladenosine of chromosome-associated regulatory RNA regulates chromatin state and transcription. Science *367*, 580–586. https://doi.org/10.1126/science.aay6018.

13. Xiao, S., Cao, S., Huang, Q., Xia, L., Deng, M., Yang, M., Jia, G., Liu, X., Shi, J., Wang, W., et al. (2019). The RNA N(6)-methyladenosine modification landscape of human fetal tissues. Nat. Cell Biol. *21*, 651–661. https://doi.org/10.1038/s41556-019-0315-4.

14. Dominissini, D., Moshitch-Moshkovitz, S., Schwartz, S., Salmon-Divon, M., Ungar, L., Osenberg, S., Cesarkas, K., Jacob-Hirsch, J., Amariglio, N., Kupiec, M., et al. (2012). Topology of the human and mouse m6A RNA methylomes revealed by m6A-seq. Nature *485*, 201–206. https://doi.org/10.1038/nature11112.

15. Meyer, K.D., Saletore, Y., Zumbo, P., Elemento, O., Mason, C.E., and Jaffrey, S.R. (2012). Comprehensive analysis of mRNA methylation reveals enrichment in 3' UTRs and near stop codons. Cell *149*, 1635–1646. https://doi.org/10.1016/j.cell.2012.05.003.

16. Xu, W., Li, J., He, C., Wen, J., Ma, H., Rong, B., Diao, J., Wang, L., Wang, J., Wu, F., et al. (2021). METTL3 regulates heterochromatin in mouse embryonic stem cells. Nature *591*, 317–321. https://doi.org/10.1038/s41586-021-03210-1.

17. Liu, J., Gao, M., He, J., Wu, K., Lin, S., Jin, L., Chen, Y., Liu, H., Shi, J., Wang, X., et al. (2021). The RNA m(6)A reader YTHDC1 silences retrotransposons and guards ES cell identity. Nature *591*, 322–326. https://doi.org/10.1038/s41586-021-03313-9.

18. Duda, K.J., Ching, R.W., Jerabek, L., Shukeir, N., Erikson, G., Engist, B., Onishi-Seebacher, M., Perrera, V., Richter, F., Mittler, G., et al. (2021). m6A RNA methylation of major satellite repeat transcripts facilitates chromatin association and RNA:DNA hybrid formation in mouse heterochromatin. Nucleic Acids Res. *49*, 5568–5587. https://doi.org/10.1093/nar/gkab364.

19. Chen, C., Liu, W., Guo, J., Liu, Y., Liu, X., Liu, J., Dou, X., Le, R., Huang, Y., Li, C., et al. (2021). Nuclear m(6)A reader YTHDC1 regulates the scaffold function of LINE1 RNA in mouse ESCs and early embryos. Protein Cell *12*, 455–474. https://doi.org/10.1007/s13238-021-00837-8.

20. Akhtar, J., Renaud, Y., Albrecht, S., Ghavi-Helm, Y., Roignant, J.Y., Silies, M., and Junion, G. (2021). m(6)A RNA methylation regulates promoter-proximal pausing of RNA polymerase II. Mol. Cell. *81*, 3356–3367.e6. https://doi.org/10.1016/j.molcel.2021.06.023.

21. Yang, X., Liu, Q.L., Xu, W., Zhang, Y.C., Yang, Y., Ju, L.F., Chen, J., Chen, Y.S., Li, K., Ren, J., et al. (2019). m(6)A promotes R-loop formation to facilitate transcription termination. Cell Res. *29*, 1035–1038. https://doi.org/10.1038/s41422-019-0235-7.

22. Śledź, P., and Jinek, M. (2016). Structural insights into the molecular mechanism of the m(6)A writer complex. Elife *5*, e18434. https://doi.org/10.7554/eLife.18434.

23. Wang, P., Doxtader, K.A., and Nam, Y. (2016). Structural basis for cooperative function of Mettl3 and Mettl14 methyltransferases. Mol. Cell. *63*, 306–317. https://doi.org/10.1016/j.molcel.2016.05.041.

24. Wang, X., Feng, J., Xue, Y., Guan, Z., Zhang, D., Liu, Z., Gong, Z., Wang, Q., Huang, J., Tang, C., et al. (2016). Structural basis of N(6)-adenosine methylation by the METTL3-METTL14 complex. Nature *534*, 575–578. https://doi.org/10.1038/nature18298.

25. Lin, Z., Hsu, P.J., Xing, X., Fang, J., Lu, Z., Zou, Q., Zhang, K.J., Zhang, X., Zhou, Y., Zhang, T., et al. (2017). Mettl3-/Mettl14-mediated mRNA N(6)-methyladenosine modulates murine spermatogenesis. Cell Res. *27*, 1216–1230. https://doi.org/10.1038/cr.2017.117.

26. Liu, P., Li, F., Lin, J., Fukumoto, T., Nacarelli, T., Hao, X., Kossenkov, A.V., Simon, M.C., and Zhang, R. (2021). m(6)A-independent genome-wide METTL3 and METTL14 redistribution drives the senescence-associated secretory phenotype. Nat. Cell Biol. *23*, 355–365. https://doi.org/10.1038/s41556-021-00656-3.

27. Barbieri, I., Tzelepis, K., Pandolfini, L., Shi, J., Millán-Zambrano, G., Robson, S.C., Aspris, D., Migliori, V., Bannister, A.J., Han, N., et al. (2017). Promoter-bound METTL3 maintains myeloid leukaemia by m(6)A-dependent translation control. Nature *552*, 126–131. https://doi.org/10.1038/nature24678.

28. Liu, J., Yue, Y., Han, D., Wang, X., Fu, Y., Zhang, L., Jia, G., Yu, M., Lu, Z., Deng, X., et al. (2014). A METTL3–METTL14 complex mediates mammalian nuclear RNA N 6-adenosine methylation. Nat. Chem. Biol. *10*, 93–95.

29. Bleckwehl, T., Crispatzu, G., Schaaf, K., Respuela, P., Bartusel, M., Benson, L., Clark, S.J., Dorighi, K.M., Barral, A., Laugsch, M., et al. (2021). Enhancer-associated H3K4 methylation safeguards in vitro germline competence. Nat. Commun. *12*, 5771. https://doi.org/10.1038/s41467-021-26065-6.

30. Villaseñor, R., Pfaendler, R., Ambrosi, C., Butz, S., Giuliani, S., Bryan, E., Sheahan, T.W., Gable, A.L., Schmolka, N., Manzo, M., et al. (2020). ChromID identifies the protein interactome at chromatin marks. Nat. Biotechnol. *38*, 728–736. https://doi.org/10.1038/s41587-020-0434-2.

31. Wang, Y., Li, Y., Yue, M., Wang, J., Kumar, S., Wechsler-Reya, R.J., Zhang, Z., Ogawa, Y., Kellis, M., Duester, G., and Zhao, J.C. (2018). N(6)-methyladenosine RNA modification regulates embryonic neural stem cell self-renewal through histone modifications. Nat. Neurosci. *21*, 195–206. https://doi.org/10.1038/s41593-017-0057-1.

32. Liu, X., Wang, H., Zhao, X., Luo, Q., Wang, Q., Tan, K., Wang, Z., Jiang, J., Cui, J., Du, E., et al. (2021). Arginine methylation of METTL14 promotes RNA N(6)-methyladenosine modification and endoderm differentiation of mouse embryonic stem cells. Nat. Commun. *12*, 3780. https://doi.org/10.1038/s41467-021-24035-6.

33. Kidder, B.L., Hu, G., and Zhao, K. (2014). KDM5B focuses H3K4 methylation near promoters and enhancers during embryonic stem cell self-renewal and differentiation. Genome Biol. *15*, R32. https://doi.org/10.1186/gb-2014-15-2-r32.

34. Peng, J.C., Valouev, A., Swigut, T., Zhang, J., Zhao, Y., Sidow, A., and Wysocka, J. (2009). Jarid2/Jumonji coordinates control of PRC2 enzymatic activity and target gene occupancy in pluripotent cells. Cell *139*, 1290–1302. https://doi.org/10.1016/j.cell.2009.12.002.

35. Galonska, C., Ziller, M.J., Karnik, R., and Meissner, A. (2015). Ground state conditions induce rapid reorganization of core pluripotency factor binding before global epigenetic reprogramming. Cell Stem Cell *17*, 462–470. https://doi.org/10.1016/j.stem.2015.07.005.

36. Zepeda-Martinez, J.A., Pribitzer, C., Wang, J., Bsteh, D., Golumbeanu, S., Zhao, Q., Burkard, T.R., Reichholf, B., Rhie, S.K., Jude, J., et al. (2020). Parallel PRC2/cPRC1 and vPRC1 pathways silence lineage-specific genes and maintain self-renewal in mouse embryonic stem cells. Sci. Adv. *6*, eaax5692. https://doi.org/10.1126/sciadv.aax5692.

37. Li, X., and Fu, X.D. (2019). Chromatin-associated RNAs as facilitators of functional genomic interactions. Nat. Rev. Genet. *20*, 503–519. https://doi.org/10.1038/s41576-019-0135-1.

38. Yoshida, A., Oyoshi, T., Suda, A., Futaki, S., and Imanishi, M. (2022). Recognition of G-quadruplex RNA by a crucial RNA methyltransferase component, METTL14. Nucleic Acids Res. *50*, 449–457. https://doi.org/10.1093/nar/gkab1211.

39. Zyner, K.G., Simeone, A., Flynn, S.M., Doyle, C., Marsico, G., Adhikari, S., Portella, G., Tannahill, D., and Balasubramanian, S. (2022). G-quadruplex DNA structures in human stem cells and differentiation. Nat. Commun. *13*, 142. https://doi.org/10.1038/s41467-021-27719-1.

40. Lyu, J., Shao, R., Kwong Yung, P.Y., and Elsässer, S.J. (2022). Genome-wide mapping of G-quadruplex structures with CUT&Tag. Nucleic Acids Res. *50*, e13. https://doi.org/10.1093/nar/gkab1073.

41. Huang, H., Weng, H., Zhou, K., Wu, T., Zhao, B.S., Sun, M., Chen, Z., Deng, X., Xiao, G., Auer, F., et al. (2019). Histone H3 trimethylation at lysine 36 guides m(6)A RNA modification co-transcriptionally. Nature *567*, 414–419. https://doi.org/10.1038/s41586-019-1016-7.

42. Dou, X., Huang, L., Xiao, Y., Liu, C., Li, Y., Zhang, X., Yu, L., Zhao, R., Yang, L., Chen, C., et al. (2023). METTL14 is a chromatin regulator independent of its RNA N6-methyladenosine methyltransferase activity. Protein Cell, pwad009. https://doi.org/10.1093/procel/pwad009.

43. Trapnell, C., Pachter, L., and Salzberg, S.L. (2009). TopHat: discovering splice junctions with RNA-Seq. Bioinformatics *25*, 1105–1111. https://doi.org/10.1093/bioinformatics/btp120.

44. Langmead, B., Trapnell, C., Pop, M., and Salzberg, S.L. (2009). Ultrafast and memory-efficient alignment of short DNA sequences to the human genome. Genome Biol. *10*, R25. https://doi.org/10.1186/gb-2009-10-3-r25.

45. Li, H., Handsaker, B., Wysoker, A., Fennell, T., Ruan, J., Homer, N., Marth, G., Abecasis, G., and Durbin, R.; 1000 Genome Project Data Processing Subgroup (2009). The sequence alignment/map format and SAMtools. Bioinformatics *25*, 2078–2079. https://doi.org/10.1093/bioinformatics/btp352.

46. Ramírez, F., Ryan, D.P., Grüning, B., Bhardwaj, V., Kilpert, F., Richter, A.S., Heyne, S., Dündar, F., and Manke, T. (2016). deepTools2: a next generation web server for deep-sequencing data analysis. Nucleic Acids Res. *44*, W160–W165. https://doi.org/10.1093/nar/gkw257.

47. Quinlan, A.R., and Hall, I.M. (2010). BEDTools: a flexible suite of utilities for comparing genomic features. Bioinformatics *26*, 841–842. https://doi.org/10.1093/bioinformatics/btq033.

48. Heinz, S., Benner, C., Spann, N., Bertolino, E., Lin, Y.C., Laslo, P., Cheng, J.X., Murre, C., Singh, H., and Glass, C.K. (2010). Simple combinations of lineage-determining transcription factors prime cis-regulatory elements required for macrophage and B cell identities. Mol. Cell. *38*, 576–589. https://doi.org/10.1016/j.molcel.2010.05.004.

49. Maeder, M.L., Linder, S.J., Cascio, V.M., Fu, Y., Ho, Q.H., and Joung, J.K. (2013). CRISPR RNA-guided activation of endogenous human genes. Nat. Methods *10*, 977–979. https://doi.org/10.1038/nmeth.2598.

50. Lan, F., Bayliss, P.E., Rinn, J.L., Whetstine, J.R., Wang, J.K., Chen, S., Iwase, S., Alpatov, R., Issaeva, I., Canaani, E., et al. (2007). A histone H3 lysine 27 demethylase regulates animal posterior development. Nature *449*, 689–694. https://doi.org/10.1038/nature06192.

51. Zhang, Y., Liu, T., Meyer, C.A., Eeckhoute, J., Johnson, D.S., Bernstein, B.E., Nusbaum, C., Myers, R.M., Brown, M., Li, W., and Liu, X.S. (2008). Model-based analysis of ChIP-seq (MACS). Genome Biol. *9*, R137. https://doi.org/10.1186/gb-2008-9-9-r137.

STAR★METHODS

KEY RESOURCES TABLE

REAGENT or RESOURCE	SOURCE	IDENTIFIER
Antibodies		
METTL14 (Used for ChIP and WB)	Sigma	Cat#HPA038002; RRID:AB_10672401
METTL14 (Used for Co-IP)	Sigma	AMAB91275, RRID:AB_2665877
EZH2	Cell Signaling	Cat##5246; RRID:AB_10694683
EED	Proteintech	Cat#16818-1-AP; RRID:AB_2262065
SUZ12	Cell Signaling	Cat#3737; RRID:AB_2196850
KDM5A	Bethyl	Cat#A300-897A; RRID:AB_2234038
KDM5B	Bethyl	Cat#A301-813A; RRID:AB_1264323
H3K27me3	Cell Signaling	Cat#9733; RRID:AB_2616029
H3K4me3	Cell Signaling	Cat#9751; RRID:AB_2616028
Actin	Proteintech	Cat#60008-1-Ig; RRID:AB_2289225
GAPDH	Proteintech	Cat#60004-1-Ig; RRID:AB_2107436
DYKDDDDK (Flag)	Smart-lifesciences	Cat.#SLAB01; RRID:N/A
HA	Cell Signaling	Cat#3724S; RRID:AB_1549585
FOXA2	Proteintech	Cat#22474-1-AP; RRID:AB_2879110
GATA6	Proteintech	Cat#55435-1-AP; RRID:AB_1118281
HOXD11	Proteintech	Cat#18734-1-AP; RRID:AB_2878558
Chemicals, peptides, and recombinant proteins		
Lipofectamine 3000	Invitrogen	Cat#L3000-015
TRIzol reagent	Invitrogen	Cat#15596018
Dynabeads Protein A/Protein G	Invitrogen	Cat#10015D
RNase A, DNase and protease-free	Thermo	Cat#EN0531
FBS	Gibco	Cat#16000-044
MEM non-essential amino acid	Gibco	Cat#11140
β-Mercaptoethanol	Gibco	Cat#21985-023
Penicillin/Streptomycin	Hyclone	Cat#SV30010
LIF	Millipore	Cat#ESG1107
CHIR99021	Selleck	Cat#S1263
PD0325901	Selleck	Cat#S1036
dTAG-13	Tocris	Cat#6605
Recombinant human FLAG-METTL14	Active Motif	Cat#31568
Recombinant human FLAG-PRC2 complex	Active Motif	Cat#31387
Recombinant human FLAG-JARID1A	Active Motif	Cat#31431
Recombinant human FLAG-JARID1B	Active Motif	Cat#31518
Nuclease P1	Thermo	Cat#18009027
Alkaline phosphatase	Sigma	Cat#P4252
HA peptide	Synthesize by Chinapeptides Co., Ltd.	N/A
Critical commercial assays		
MinElute PCR Purification Kit	Qiagen	Cat#28006
FastStart Universal SYBR Green Master (Rox)	Roche	Cat#4913914001
TURBO DNA-free Kit	Invitrogen	Cat#AM1970
PrimeScript RT reagent kit	Takara	Cat#RR047A
SYBR Premix ExTaq	Takara	Cat#RR420Q
ACCEL-NGS 2S PLUS DNA LibraryKit	SWIFT	Cat#21096
Dynabeads™ mRNA Purification Kit	Invitrogen	Cat#0067112

(*Continued on next page*)

Continued

REAGENT or RESOURCE	SOURCE	IDENTIFIER
Deposited data		
Raw and analyzed data	This paper	GEO: GSE206735
Original western blot images	This paper	https://data.mendeley.com/datasets/2yhp3dw4sk
H3K4me1, H3K4me2, H3K4me3, H3K9me3, H3K27me3, H3K27ac	(Bleckwehl et al.[29])	GSE155062
METTL3 ChIP-seq	(Xu et al.[16])	GSE126243
KDM5A ChIP-seq	(Peng et al.[34])	GSE18776
KDM5B ChIP-seq	(Kidder et al.[33])	GSE53087
Parental and Eed KO RNA-seq	(Galonska et al.[35])	GSE56312
Parental and Eed KO RNA-seq	(Zepeda-Martinez et al.[36])	GSE136584
Experimental models: Cell lines		
E14Tg2a murine embryonic stem cells (mESCs)	Gift from Qi-Long Ying, USC	N/A
HEK293T	ATCC	N/A
Oligonucleotides		
Primers for qPCR	This paper	See Table S2
Primers for cloning	This paper	See Table S2
Recombinant DNA		
Plasmid: PPB-METTL14 (WT)	This paper	N/A
Plasmid: PPB-METTL14 (R298A)	This paper	N/A
Plasmid: PPB-METTL14 (D312A)	This paper	N/A
Plasmid: METTL14 Knock In	This paper	N/A
Software and algorithms		
Tophat2	(Trapnell et al.[43])	https://ccb.jhu.edu/software/tophat/index.shtml
Bowtie	(Langmead et al.[44])	http://bowtie-bio.sourceforge.net/index.shtm
Samtool	(Li et al.[45])	http://www.htslib.org/doc/samtools.html
Deeptools	(Ramirez et al.[46])	https://deeptools.readthedocs.io/en/develop/
Bedtools	(Quinlan and Hall.[47])	http://bedtools.readthedocs.io/en/latest
Homer	(Heinz et al.[48])	http://homer.ucsd.edu/

RESOURCE AVAILABILITY

Lead contact

Further information and requests for resources and reagents may be directed to and will be fulfilled by the Lead Contact, Hongjie Shen (hongjieshen@fudan.edu.cn).

Materials availability

All unique/stable reagents generated in this study are available from the lead contact with a completed Materials Transfer Agreement. It's worth noting that the endogenous METTL14 Rabbit Polyclonal antibody used for ChIP experiments in this study (Sigma, Cat#HPA038002; RRID: AB_10672401; lot: B106302) is no longer commercially available. We have tested other lots (C118715, E115616, E107157) under the same catalog number, which did not work under our current ChIP condition. It would be important for others to perform preliminary experiments to make sure the METTL14 antibody is suitable for ChIP experiments.

Data and code availability

- ChIP-seq and RNA-seq data have been deposited at NCBI GEO repository and are publicly available as of the date of publication. Accession numbers are listed in the key resources table. This paper analyzes existing, publicly available data. These accession numbers for the datasets are listed in the key resources table.
- This paper does not report original code.
- Any additional information required to reanalyze the data reported in this paper is available from the lead contact upon request.

EXPERIMENTAL MODEL AND STUDY PARTICIPANT DETAILS

Cell culture

E14Tg2a murine embryonic stem cells (mESCs, gift from Qi-Long Ying, USC) were cultured in Dulbecco's Modified Eagle's Medium (DMEM) supplemented with 10% FBS (Gibco, #16000-044), 1% MEM non-essential amino acid (Gibco, #11140), 55 mM β-Mercaptoethanol (Gibco, #21985-023), 100 U/mL Penicillin/Streptomycin (Hyclone, #SV30010), 1000 units/mL LIF (Millipore, #ESG1107) and MEK inhibitor PD0325901 (1 μM) and GSK3β inhibitor CH99021 (3 μM) at 37°C with 5% CO_2.

METHOD DETAILS

Construction of stable cell lines and knockdown

CRISPR-Cas9 gene targeting was carried out as previously described[49] and the single knockout clones were isolated and then confirmed by Western blot showing undetectable protein. *Mettl14* KO cells were generated in our previous study.[16]

For rescued cells, cDNA of full-length murine METTL14 WT (NCBI RefSeq: NM_201638.2) or METTL14 mutation (R298A, D312A) were cloned into the pPB-CAG-IRES-Pac plasmid (Puromycine resistant). These plasmids were individually co-transfected into mESCs with pCMV-PBase plasmid in a 1:1 ratio using Lipofectamine 3000 (Invitrogen, #L3000-015) according to the manufacturer's instruction. Medium was replaced by fresh media with 2 μg/mL Puromycine after 48 h post-transfection. After continuous selection for 5 days, the surviving mESCs were pooled as stable rescued cell lines.

TAP purification of METTL14 protein complex

In brief, HA-METTL14 stably expressing *Mettl3* KO mES cells was established using pPB system as described above. mESCs nuclear extract was incubated with anti-HA and pre-washed protein A/G beads in the binding buffer (50 mM Tris-HCl pH 7.9, 150 mM KCl, 5 mM MgCl2, 0.2 mM EDTA, 20% glycerol, 0.1% NP-40, 3 mM β-ME, protease inhibitors) for 6 h, and then washed with the same buffer and eluted with HA peptides (Chinapeptides Co., Ltd.). The purified protein complex was subjected to liquid chromatography-tandem mass spectrometry (LC-MS/MS) analysis (TIMS-TOF Pro, Bruker Daltonics, Billerica, MA).

Co-immunoprecipitation

mESCs were washed once with PBS and lysed in buffer A (10 mM HEPES pH7.5, 1.5 mM $MgCl_2$, 10 mM KCl, 0.5 mM DTT, 1mM PMSF and 1x Protease Inhibitor Cocktail) on ice for 15 min, then NP-40 was added to a final concentration of 0.25% for another 5 min. Nuclei were collected by centrifugation (2,000 rpm, 3 min, 4°C) and re-suspended in buffer C (20 mM HEPES, pH 7.5, 10% Glycerol, 0.42 M KCl, 4 mM $MgCl_2$, 0.2 mM EDTA, 0.5 mM DTT, 1 mM PMSF and Protease Inhibitor Cocktail). After 30 min incubation on ice, nuclear extract was collected by high speed centrifugation (13,000 rpm, 15 min, 4°C) as nuclear extract A. Insoluble chromatin fraction was re-suspended with buffer A (2X volumes of buffer C) with DNase I. After 30 min incubation at 37°C, the soluble fraction was collected by high speed centrifugation (13,000 rpm, 15 min, 4°C) as nuclear extract B. Nuclear extract A and nuclear extract B were mixed and incubated with indicated antibody or IgG for 6 h at 4°C, followed by the addition of Dynabeads protein A/G for another 2 h. The beads were washed for 4 times with wash buffer (Mixture of buffer A and buffer C in a ratio of 2:1). SDS buffer was directly added to the beads and boiled for 10 min. The samples were loaded on SDS-PAGE gels and subjected to immunoblotting using indicated antibodies.

Genome editing for dTAG endogenous knock-in

To generate dTAG-Mettl14 and cells by the endogenous knock-in, PITCh plasmids (sgRNA cutting and microhomology-containing dTAG repair template plasmid) were co-transfected into mESCs (See Table S2 for oligo sequences). After recovering for 2 days without antibiotic selection, cells were serially diluted and cultured with 2 μg/mL puromycin for 5 days. Single-clone colonies were picked, expanded, and genotyped by genomic DNA PCR targeting the integration site. For homogeneous knock-in clones, protein degradation efficiency was verified by dTAG-13 (Tocris, #6605) treatment for 12 h followed by western blotting.

In vitro pull-down

For protein-protein interaction assays, we used recombinant human FLAG-METTL14 (Active Motif, #31568), recombinant human FLAG-PRC2 complex (Active Motif, #31387), recombinant human FLAG-JARID1A (Active Motif, #31431), recombinant human FLAG-JARID1B (Active Motif, #31518). A total of 1μg FLAG-METTL14, 2 μg anti-METTL14/IgG and protein A/G beads were incubated in 200μL binding system (50 mM Tris-HCl pH 7.9, 150 mM KCl, 5 mM MgCl2, 0.2 mM EDTA, 20% glycerol, 0.1% NP-40, 3 mM β-ME, protease inhibitors). After 1h incubation at 4°C, beads were washed 5 times with binding buffer, and then add 1ug FLAG-PRC2/KDM5A/KDM5B. After 2h incubation at 4°C, beads were washed 5 times with binding buffer, and then boiled for 10 min in 50 μL of SDS loading buffer for Western blotting analysis.

Isolation of mRNA for QQQ and HPLC analysis

mRNA was isolated from 5μg total RNA followed with Dynabeads™ mRNA Purification Kit (Invitrogen, #0067112). Purified mRNA was digested by nuclease P1 (Thermo, #18009027) in 25 μL of buffer containing 25 mM NaCl and 2.5 mM of $ZnCl_2$ at 42°C for 2 h, which was followed by addition of NH_4HCO_3 (1 M, 3μL) and alkaline phosphatase (Sigma, #P4252) and additional incubation at 37°C for 2 h. Samples were then diluted to 60 μL and 5 μL of solution was loaded into liquid chromatography-tandem mass spectrometry (LC-MS/MS) (Sciex 4000Qtrap).

ChIP-seq

ChIP assays were performed as described elsewhere.[50] Briefly, chromatin samples were incubated with specific antibodies in the ChIP lysis buffer (20 mM Tris-HCl pH 8.1, 150 mM NaCl, 2 mM EDTA, 1% Triton X-100 and 0.05% SDS) overnight at 4°C. The protein-DNA complexes were immobilized on pre-washed protein A/G beads. The bound fractions were washed 3 times with the Lysis buffer, and twice with the Low Salt Wash buffer (10 mM Tris-HCl, 250 mM LiCl, 1 mM EDTA, 0.5% NP-40, 0.5% Na-deoxylcholate), and once with 10 mM Tris-HCl pH8.0. Elution and reverse crosslinking were carried out in the Elution buffer (50 mM Tris-HCl pH8.0, and 1% SDS) at 65°C for 5 h. After 1 h of RNase A (1 unit/μl) at 37°C and Proteinase K (1 unit/μl) digestion at 55°C, DNA samples were then purified using PCR extraction kit (QIAGEN, #28006). The precipitated DNA samples were prepared for DNA deep sequencing according to manufacturer's guidelines (SWIFT, #21096).

For histone modifications ChiP-seq in Mettl14 KI cells, ChIP-Rx was conducted. Human HEK293T cells processed identically as spike-in for normalization.

RT-qPCR

Total RNAs from mESCs were isolated using TRIzol reagent (Invitrogen, #15596018) and treated with TURBO DNase using TURBO DNA-free Kit (Invitrogen, #AM1970) according to the manufacturer's instruction. cDNAs were synthesized with PrimeScript RT reagent kit (Takara, #RR047A) containing random primers using 1μg of RNA per sample. RT-qPCR was performed using SYBR Premix ExTaq (Takara, #RR420Q) with the Roche Lightcycler 480 Instrument II system. Primer sequences are listed in Table S2.

Western blots

SDS loading buffer was added to the samples directly and boiled for 10 min. The samples were loaded on SDS-PAGE gels and transferred from the gel to the membrane. Block the membrane for 1 h at room temperature using blocking buffer (5% milk in PBST). Incubate the membrane with appropriate dilutions (presented below) of primary antibody in blocking buffer overnight incubation at 4°C. Wash the membrane in three washes of PBST, 5 min each. Incubate the membrane with the recommended dilution of conjugated secondary antibody in blocking buffer at room temperature for 1 h. Wash the membrane in three washes of PBST, 5 min each. For signal development, follow the kit manufacturer's recommendations and remove excess reagent. The intensity of the band was measured by Bio-Rad Image Lab software (Bio-rad). Primary antibodies concentrations used are as below: anti-METTL14 (1:1000, Sigma); anti-ACTIN (1:1000, Proteintech); anti-GAPDH (1:1000, Proteintech); EZH2 (1:1000, Cell Signaling); EED (1:1000, Proteintech); SUZ12 (1:1000, Cell Signaling); KDM5A (1:1000, Bethyl); KDM5B (1:1000, Bethyl); DYKDDDDK (Flag) (1:1000, Smart-lifesciences); HA (1:1000, Cell Signaling); HA-HRP (1:1000, Cell Signaling); FOXA2 (1:1000, Proteintech); GATA6 (1:1000, Proteintech); HOXD11 (1:1000, Proteintech).

Strand specific total RNA-seq

Strand specific total RNA library preparation was performed using NEBNext Ultra Directional RNA Library Prep Kit for Illumina (NEB, #E7420S).

QUANTIFICATION AND STATISTICAL ANALYSIS

ChIP-seq analysis

Raw reads were aligned to the mm10 genome using Bowtie2[44] (v2.2.5) to report best alignment. PCR duplicates were removed using samtools[45] (v1.11) rmdup. Genome coverage bedGraph files for UCSC genome browser were generated by deeptools[46] (v2.5.7) bamCoverage with the parameters "-of bedgraph –normalizeUsingRPKM –binSize 25" for UCSC track. Peaks were generated by macs2[51] (2.1.4) callpeak with parameters "-p 0.00001 –nomodel -f BAMPE". Peak annotation was carried out using Homer[48] (v4.8.2) annotatePeaks.pl. The Jaccard statistic representing the ratio of the intersection of two sets to the union of the two sets is calculated using bedtools[47] (v2.26.0). Genome coverage bigwig files for heatmap and aggregation plot were generated by deeptools[46] (v2.5.7) bamCoverage with the parameter "–normalizeUsingRPKM –binSize 5". Heatmaps were generated by deeptools[46] (v2.5.7) computeMatrix and plotHeatmap. Aggregation plots were generated by deeptools[46] (v2.5.7) computeMatrix and plotProfile. ChIP-seq density on bivalent domains were calculated by Homer[48] (v4.8.2) analyzeRepeats.pl. Boxplot were generated by R boxplot. Log2 transformed fold change is generated by deeptools[46] (v2.5.7) bamCompare with the parameter "–binSize 5" and scaleFactors as the following.

Mettl14 KO/Parental	ScaleFactor
METTL14	0.923
H3K27me3	1.105
H3K4me3	1.106

For public ChIP-seq data, Peaks were generated by macs2[51] (2.1.4) callpeak with parameters "-p 0.00001 –nomodel -f BAM".

For ChIP-Rx analysis, The paired-end ChIP-Rx reads were processed with Trim Galore v0.6.6 (https://www.bioinformatics.babraham.ac.uk/projects/trim_galore/) to remove adaptors and then aligned to the human hg19 and mouse mm10 assemblies using Bowtie2[44] (v2.2.5) with default parameters. PCR duplicates were removed using samtools[45] (v1.11) rmdup. The number of spike-in mm10 reads was counted with samtools[45] (v1.11) and normalization factor alpha = 1e6/mm10_count was calculated.

Total RNA-seq analysis

Raw reads were aligned to the mm10 genome using TopHat[43] (v2.1.1). Genome coverage bedGraph files for UCSC genome browser were generated by deeptools[46] (v2.5.7) bamCoverage with the parameters "-of bedgraph –normalizeUsingRPKM –binSize 5". Genome coverage bigwig files for RNA-seq were generated by deeptools[46] (v2.5.7) bamCoverage with the parameter "–normalizeUsingRPKM –binSize 5". RNA-seq density on bivalent genes were calculated by Homer[48] (v4.8.2) analyzeRepeats.pl. Boxplot were generated by R boxplot.

Analyses of repeats correlation

Correlation between sequencing sample repeats are calculated with deeptools[46] (v2.5.7). Briefly, coverage on every 10kb bins across genome are calculated with multiBigwigSummary, and pearson correlation test are carried out using plotCorrelation. Pearson correlation coefficients for the biological replicates are listed in Table S3.